# Rigorous Analysis of Light Diffraction Ellipsometry by Striated Muscle Fibers

E. Sidick,* R. J. Baskin,‡ Y. Yeh,§ and A. Knoesen*
Departments of *Electrical and Computer Engineering, ‡Molecular and Cellular Biology, and §Applied Science, University of California, Davis, California 95616 USA

ABSTRACT A rigorous analysis of both the transverse electric and the transverse magnetic modes of light diffracted from a muscle fiber is performed. From the expressions of electromagnetic field components, ellipsometry parameters, differential field ratio, $r$, and birefringence, $\Delta n$, have been obtained. A theoretical formulation that introduces myofibril skew planes and a randomization factor about the average skew plane yields a relationship that shows good fit to experimental data of Chen et al. (*Biophys. J.* 56:595, 1989) and Burton et al. (*J. Muscle Res. Cell Motil.* 11:258, 1990). Using indices of refraction within each of the regions of the sarcomeric unit that are consistent with our knowledge of the molecular structure of the sarcomere in the analysis, it is shown that the transition from the rigor state to the resting state leads to as much as a ~13% decrease in the $r$-value and an equally significant change in $\Delta n$.

## INTRODUCTION

Optical ellipsometry has been successfully applied to the study of the structure and dynamics of skeletal muscle fibers in at least two experimental configurations. The passage of light with a well defined state of polarization through a muscle fiber that is optically anisotropic will lead to measurable *transmission* birefringence. This phenomenon was exploited in muscle research by Eberstein and Rosenfalck (1963), Colby (1971), and Taylor (1975). The theoretical basis of form birefringence by a muscle fiber was analyzed by Haskell et al. (1989). Recent birefringence experiments by Irving et al. (1987) and Peckham and Irving (1989) examined the changes in the states of fibers. That light *diffracted* by a single muscle fiber also exhibits optical anisotropic properties was noted by Yeh et al. (1983, 1985), Baskin et al. (1986), and Leung et al. (1987). An analysis of the polarization characteristics of light diffracted by muscle fibers developed by Yeh and Baskin (1988) was based on single scattering of light by an optically anisotropic grating, and as such, does not take into account the more complex mode coupling between different diffraction orders. In search for a more comprehensive treatment of this problem, our group developed a rigorous analysis to describe the diffraction of light by a striated muscle fiber (Sidick et al., 1992), this reference hereafter known as (I), based on a rigorous coupled-wave theory (Moharam and Gaylord, 1982, 1983; Gaylord and Moharam, 1985). Results of this analysis were compared with the normal mode analysis by Huxley (1990) and the multiwave first-order coupled-wave approximation of Thornhill et al. (1991). We now extend this analysis to account for both the transverse electric (TE) and the transverse magnetic (TM) electromagnetic field components. The ability to treat both types of polarization allows for a complete analysis of optical anisotropy of the muscle fiber. From such an analysis, a rigorous study of diffracted light that includes its polarization properties and the changes thereof is shown to account for many of the observed experimental features.

*Received for publication 20 December 1993 and in final form 15 March 1994.*

Address reprint requests to Dr. Yin Yeh, Department of Applied Science, University of California–Davis, Davis, CA 95616. Tel.: 916-752-1924; Fax: 916-752-2444; E-mail: yyeh@raphael.engr.ucdavis.edu.



0006-3495/94/06/2051/11 $2.00

## MATERIALS AND METHODS

### Optical model of muscle fiber

In our model, the muscle fiber is represented by a large number of stacked slabs of dielectric material (Fig. 1 *a*), and each has an identical periodic structure. The basis of the periodicity is that a single myofibril, here represented by a slab, has longitudinal sarcomeric periodicity along the fiber, and that all the myofibrils lying in each slab are assumed to be identical. Within each sarcomeric unit, there are optically anisotropic myosin molecules that form the thick filament of a fixed length $a$. There are (assumed) isotropic F-actin filaments each of length $b/2$, and each connected to a Z-band of thickness $\zeta$. The combination of these lengths makes up the sarcomere length $\Lambda$ (Fig. 1 *b*). Sarcomere length changes are effected by the sliding of thin filaments relative to the thick filaments. Consistent with the sliding filament model (Huxley and Niedergerke, 1957), the lengths of all filaments are assumed to be constant.

The basis for the assignment of values of indices of refraction for each of these regions is the same as that which was previously described by Yeh and Baskin, and later refined in the work of Chen et al. (1989) and Jones et al. (1991). The values of the indices of refraction in the different regions within the sarcomere are tabulated in Table 1. As filaments slide relative to each other, the degree of optical anisotropy will change. In addition, within the overlap region of the thick and thin filaments, the S-1 and S-2 cross-bridges make distinct contributions. Form anisotropy was first postulated to be the basis for significant changes in optical birefringence of protein solutions by Bragg and Pippard (1953). The theoretical analysis developed by Haskell et al. (1989) for a single muscle fiber is consistent with this idea. In our formulation, we incorporated the fact that the thick filaments include not only the optically anisotropic myosin rod (light meromyosin (LMM) and subfragment-2 (S-2)), but that individual optically isotropic subfragments-1 (S-1) have different averaged orientations depending on the state of the fiber. We imposed changes in the indices of refraction of the A-band material in accordance with the postulated change in form contribution of optical anisotropy derived from a combination of orientational changes of S-1 and S-2

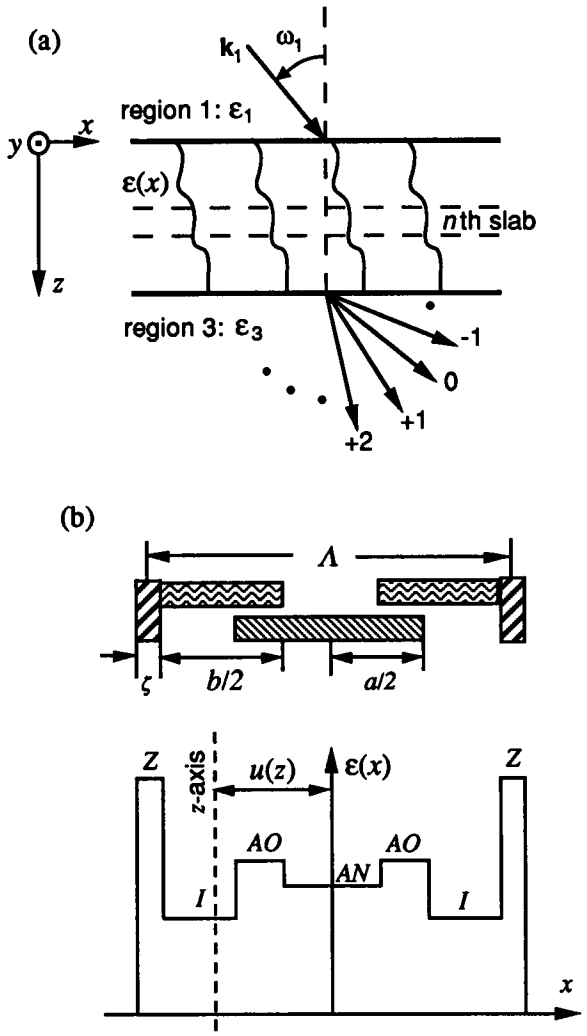


FIGURE 1 (*a*) Two dimensional geometry of a muscle fiber represented by a dielectric phase grating with an arbitrary striation pattern where distinct indices of refraction divide the regions. Light is incident from region 1 into the grating region at an angle $\omega_1$. The grating region is divided into thin slabs (representing myofibrils) of which the *n*th slab is indicated. (*b*) Schematic diagram of the sarcomeric unit of a muscle fiber. The sarcomere length is given by $\Lambda$. The A-band has a fixed length *a*, and each thin filament of I-band has a length *b*/2. The relative permittivities of nonoverlapping A-band, overlapping A-band, I-band, and Z-line are indicated in the lower diagram by *AN*, *AO*, *I*, and *Z*, respectively. The thickness of the *Z*-line is $\zeta$, and $u(z)$ is the distance between the center of a sarcomeric unit and the *z* axis.

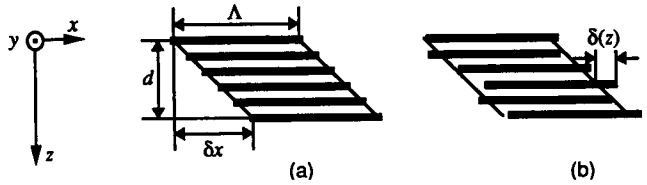


FIGURE 2 (*a*) The presence of myofibrillar skew is represented by slip plane defined by a distance $\delta x$ along the fiber axis (*x*-direction) across the thickness *d* of the fiber. (*b*) The random variable $\delta(z)$ quantifies the randomness associated with a particular myofibril relative to the average slip plane.

subfragments. Geometric constraints will impose a 10° maximum angle of tilt for the S-2 elements. As for S-1 subfragments, we assume that rigid cross-bridges in the rigor state make an angle of 68° from the fiber axis. This assumed angle is larger than the angles of rigor S-1 moieties as determined by Pollard et al. (1993) by direct EM visualization, but is more consistent with our experimental data (Chen et al., 1989). The relaxed fiber is in a state where no cross-bridges make contact with the thin filament. Accordingly, we imposed a random distribution of these S-1 subfragments. This assumption is reasonably consistent with the EM results of Pollard et al. In the rapidly frozen cross-bridges in ATP-activated states, Hirose et al. (1993) found that the cross-bridges are randomly distributed. Because dynamic spin probe measurements (Fajer et al., 1990) indicate that a small fraction (10–20%) of the S-1 heads are rigor-like during isometric contraction, we have placed a constraint on the active state: 20% of the cross-bridges are bound while the remaining 80% remain in a random, unbound configuration; for those cross-bridges that are bound, we assumed that they possess the rigor binding configuration.

One other parameter that is left as a variable in the present analysis is the fact that adjacent myofibrils (slabs) may actually have "slippage" or misalignment with respect to its previous layer. This is illustrated in Fig. 2, where in *a*, a regular slip of distance $\delta x$ has been imposed over the thickness *d* of the fiber grating. In *b*, we imposed a further condition that the slippage between adjacent slabs could be somewhat random. The degree of randomness is given by $\delta(z)$. This is to say that as we progress through the fiber, myofibrils not only have an average slip plane, but the actual amount of slippage may be randomly distributed about that averaged slip plane. The maximum value of the randomness in slip plane is given by $\delta_0$ in a function $\delta(z) = \delta_0\,\mathrm{rand}(z)$, where $\mathrm{rand}(z)$ is a random variable uniformly distributed in the interval $[-\frac{1}{2}, \frac{1}{2}]$.

## General remarks about the theory

We used the rigorous coupled-wave theory (Moharam and Gaylord, 1982, 1983; Gaylord and Moharam, 1985) in our analysis. The basis of this theory has been discussed in detail in (I). Briefly, as electromagnetic wave propagates through the *n*th dielectric slab of thickness $z_0$, it will encounter boundaries at $z_{n-1}$ and $z_n$. At each boundary, the fields will have to satisfy appropriate boundary conditions for the two types of polarization, TE and TM. Appropriate changes in the fields that are transmitted or reflected are then accounted for across each slab. In the event that the medium is a striated one of periodicity $\Lambda$, coherent reinforcements of the diffraction orders occur at each slab. These, in turn, are accounted for in the propagation of the waves into the next slab. In this manner, each order of the diffracted waves from a single slab region will couple into the next slab with a differing amount of efficiency. We hasten to emphasize that the present model is really a two-dimensional model where the *y*-direction is assumed to be of infinite extent. There is no myofibrillar structure or randomness in the *y*-direction. As such, principal optic axis of the fiber dielectric is the fiber axis, which is the *x* axis in Fig. 1 *a*, and the TE and TM waves do not couple with each other when propagating inside the fiber. This is an approximation that is reasonable if the incident beam has a beam diameter that is small as compared with the fiber diameter, and the collection optics samples only the meridional pattern.

Because the TE and the TM waves (here they are equivalent to ordinary and extraordinary waves) decouple from each other in the present case, the diffraction problem reduces to the two fundamental cases of polarization (TE and TM) that may be treated separately. The case of TE polarization has already been treated in detail in (I); therefore, we restrict our analysis here to only the TM polarization. Furthermore, considering the similarities between the analytical procedures of the two cases of polarization, we will only briefly outline the formulation of TM wave diffraction and present the final results.

## Matrix formulation of rigorous coupled-wave theory for TM polarization

Consider a uniform plane wave incident in the *xz* plane from region 1 with an arbitrary angle $\omega_1$ into a grating (Fig. 1 a). The magnetic field of the wave

**TABLE 1 Indices of refraction for the different regions of a sarcomere as functions of sarcomere length Λ**

| | | Regions within a sarcomere | | | | | |
|---|---|---|---|---|---|---|---|
| | Λ (μm) | AN | I | Z | AO (rig) | AO (rel) | AO (act) |
| $\sqrt{\epsilon} = n_\perp$ | 2.2 | 1.3489 | 1.3460 | 1.3632 | 1.3587 | 1.3587 | 1.3587 |
| | 2.3 | 1.3506 | 1.3460 | 1.3641 | 1.3587 | 1.3587 | 1.3587 |
| | 2.4 | 1.3515 | 1.3460 | 1.3649 | 1.3589 | 1.3588 | 1.3588 |
| | 2.5 | 1.3521 | 1.3461 | 1.3658 | 1.3591 | 1.3591 | 1.3591 |
| | 2.6 | 1.3527 | 1.3462 | 1.3667 | 1.3595 | 1.3594 | 1.3594 |
| | 2.7 | 1.3533 | 1.3464 | 1.3675 | 1.3600 | 1.3600 | 1.3600 |
| | 2.8 | 1.3540 | 1.3467 | 1.3684 | 1.3607 | 1.3606 | 1.3607 |
| | 2.9 | 1.3548 | 1.3470 | 1.3693 | 1.3616 | 1.3615 | 1.3615 |
| | 3.0 | 1.3557 | 1.3473 | 1.3702 | 1.3626 | 1.3626 | 1.3626 |
| | 3.1 | 1.3567 | 1.3478 | 1.3711 | 1.3640 | 1.3639 | 1.3639 |
| | 3.2 | 1.3580 | 1.3484 | 1.3721 | 1.3656 | 1.3655 | 1.3655 |
| | 3.3 | 1.3596 | 1.3491 | 1.3730 | 1.3676 | 1.3675 | 1.3675 |
| | 3.4 | 1.3616 | 1.3500 | 1.3741 | 1.3701 | 1.3700 | 1.3700 |
| | 3.5 | 1.3640 | 1.3512 | 1.3751 | 1.3732 | 1.3731 | 1.3731 |
| | 3.6 | 1.3671 | 1.3527 | 1.3763 | 1.3770 | 1.3769 | 1.3770 |
| $\sqrt{\kappa} = n_\parallel$ | 2.2 | 1.3503 | 1.3467 | 1.3597 | 1.3609 | 1.3610 | 1.3610 |
| | 2.3 | 1.3520 | 1.3467 | 1.3604 | 1.3609 | 1.3610 | 1.3610 |
| | 2.4 | 1.3529 | 1.3467 | 1.3611 | 1.3610 | 1.3611 | 1.3611 |
| | 2.5 | 1.3536 | 1.3468 | 1.3619 | 1.3613 | 1.3614 | 1.3614 |
| | 2.6 | 1.3542 | 1.3470 | 1.3626 | 1.3617 | 1.3618 | 1.3618 |
| | 2.7 | 1.3549 | 1.3472 | 1.3634 | 1.3623 | 1.3624 | 1.3624 |
| | 2.8 | 1.3556 | 1.3474 | 1.3642 | 1.3630 | 1.3632 | 1.3631 |
| | 2.9 | 1.3564 | 1.3478 | 1.3649 | 1.3640 | 1.3641 | 1.3641 |
| | 3.0 | 1.3574 | 1.3482 | 1.3657 | 1.3652 | 1.3653 | 1.3653 |
| | 3.1 | 1.3586 | 1.3487 | 1.3665 | 1.3666 | 1.3668 | 1.3667 |
| | 3.2 | 1.3600 | 1.3494 | 1.3673 | 1.3684 | 1.3686 | 1.3685 |
| | 3.3 | 1.3617 | 1.3502 | 1.3682 | 1.3706 | 1.3708 | 1.3707 |
| | 3.4 | 1.3638 | 1.3512 | 1.3690 | 1.3733 | 1.3735 | 1.3734 |
| | 3.5 | 1.3665 | 1.3525 | 1.3700 | 1.3767 | 1.3769 | 1.3768 |
| | 3.6 | 1.3698 | 1.3542 | 1.3710 | 1.3809 | 1.3811 | 1.3810 |

AO region is the overlap region between A-band and I-band. Due to the presence of S-1 and S-2 moieties, indices within this region are subject to change depending on the state of the muscle: rig, rigor state; rel, relaxed state; act, activated state. Data were generated using the fiber parameters given by Yeh and Baskin (1988) for $\lambda_o$ = 633 nm and based on the discussions contained herein.

is perpendicular to the plane of incidence ($xz$ plane), and all field components have harmonic time dependence $\exp(j\Omega t)$, where $\Omega$ is the angular frequency of the wave. Inside an anisotropic medium, the electric field intensity $\vec{E}$ is related to the displacement current density $\vec{D}$ through the relation $\vec{D} = \epsilon_o\bar{\epsilon}\vec{E}$, where $\bar{\epsilon}$ is the relative permittivity tensor of the medium. In the present case $\bar{\epsilon}$ is diagonal with its on-diagonal elements $\epsilon_{11} = \kappa$ and $\epsilon_{22} = \epsilon_{33} = \epsilon$, where $\epsilon$ and $\kappa$ denote the ordinary (perpendicular, $\epsilon_\perp$) and extraordinary (parallel, $\epsilon_\parallel$) relative permittivities, respectively.

We now describe the formulation of the problem for the $n$th slab. For clarity, we suppress a subscript $n$ labeling the numbers of different layers from all quantities. Substituting $\vec{D} = \epsilon_o\bar{\epsilon}\vec{E}$ into the Maxwell's equations, we obtain relationships among electric and magnetic fields for TM wave ($E_x$, $E_z$, $H_y$) inside the $n$th slab of the grating as

$$\frac{\partial E_x}{\partial z} - \frac{\partial E_z}{\partial x} = -j\Omega\mu_o H_y, \tag{1a}$$

$$\frac{\partial H_y}{\partial z} = -j\Omega\epsilon_o\kappa(x)E_x, \tag{1b}$$

$$\frac{\partial H_y}{\partial x} = j\Omega\epsilon_o\epsilon(x)E_z. \tag{1c}$$

Note that unlike the TE case where only $\epsilon$ is involved, in the case of TM wave, both $\epsilon$ and $\kappa$ are needed in the analysis. Because $\epsilon$ and $\kappa$ are periodic, that is, $\gamma(x + \Lambda) = \gamma(x)$ with $\gamma = \epsilon$ or $\kappa$, each can be expanded into a Fourier series

$$\gamma(x) = \sum_{h=-\infty}^{+\infty} \hat{\gamma}_h e^{jhKx}, \tag{2}$$

where $K = 2\pi/\Lambda$ is the magnitude of the grating vector, $\Lambda$ is the grating period, and $\hat{\gamma}_h = \hat{\epsilon}_h$ or $\hat{\kappa}_h$ are the complex Fourier series coefficients, which are obtained from

$$\hat{\gamma}_h = \frac{1}{\Lambda}\int_{-\Lambda/2}^{\Lambda/2} \gamma(x)e^{-jhKx}\,dx. \tag{3}$$

For the grating profile shown in Fig. 1 $b$, $\hat{\gamma}_h$ take the following forms:

$$\hat{\gamma}_h = \frac{1}{\Lambda}\gamma_{AN}a + \gamma_I b + \gamma_Z\zeta + (\gamma_{AO} - \gamma_{AN} - \gamma_I)\Delta x], \quad \text{for } h = 0, \tag{4a}$$

$$\hat{\gamma}_h = \frac{e^{-jhKu(z)}}{\pi h}\left[(\gamma_{AN} - \gamma_{AO})\sin\left(\pi h\frac{a - \Delta x}{\Lambda}\right) + (\gamma_{AO} - \gamma_I)\sin\left(\pi h\frac{a}{\Lambda}\right) + (\gamma_Z - \gamma_I)\sin\left(\pi h\frac{\zeta}{\Lambda}\right)\cos(\pi h)\right], \quad \text{for } h \neq 0, \tag{4b}$$

where $u(z)$ is the distance between the center of permittivity profile and the $z$ axis, as shown in the lower part of Fig. 1 $b$, and $\Delta x$ is the total width of the overlap A-band within one grating period and related to $\Lambda$ by $\Lambda = a + b + \zeta - \Delta x$. In (4), $\gamma$ is replaced by $\epsilon$ or $\kappa$ when calculating $\hat{\epsilon}_h$ or $\hat{\kappa}_h$.

Inside the grating, the electromagnetic fields are represented as the sum of space harmonics, that is,

$$E_x = \sum_{i=-\infty}^{+\infty} e_{xi}(z)e^{-j\sigma_i kx}, \tag{5a}$$

$$E_z = \sum_{i=-\infty}^{+\infty} e_{zi}(z)e^{-j\sigma_i kx}, \tag{5b}$$

$$H_y = \sqrt{\epsilon_o/\mu_o}\sum_{i=-\infty}^{+\infty} h_i(z)e^{-j\sigma_i kx}, \tag{5c}$$

where $\sigma_i = n_1 \sin \omega_1 - i\lambda/\Lambda$, $k = 2\pi/\lambda$, $n_1$ is the refractive indices of region 1, $\lambda$ is the free space wavelength, and $i$ is an integer labeling the diffraction orders. Substituting (2) and (5) into (1), performing the indicated differentiations, and setting the coefficient of each exponential term equal to zero, we obtain the following first-order coupled-wave equations:

$$\frac{de_{xr}(z)}{dz} = -jk[\sigma_i e_{zr}(z) + h_r(z)], \tag{6a}$$

$$\frac{dh_r(z)}{dz} = -jk \sum_{h=-\infty}^{+\infty} \hat{\kappa}_h e_{x,r-h}(z), \tag{6b}$$

$$\sigma_i h_r(z) = -\sum_{h=-\infty}^{+\infty} \hat{\epsilon}_h e_{z,r-h}(z), \tag{6c}$$

where the subscript $r$ corresponds to the space harmonics and runs from 1 to $s$ when $i$ is varied from $-i_1$ to $i_2$ (both $i_1$ and $i_2$ are positive integers), and $s$ is the total number of space harmonics retained in calculation. If we define the $s$-dimensional column vectors

$$\vec{\Psi}(z) = [\Psi_1(z) \quad \Psi_2(z) \quad \cdots \quad \Psi_s(z)]^T \tag{7}$$

with $\vec{\Psi} = \{\vec{e}_x, \vec{e}_z, \vec{h}_y\}$, $\Psi_r = \{e_{xr}, e_{zr}, h_{yr}\}$, and with superscript $T$ indicating the matrix transpose, then the following coupled-wave equations about the amplitudes of tangential space harmonics are obtained:

$$\frac{d\vec{e}_x}{dz} = -jk\vec{B}\vec{h}_y, \tag{8a}$$

$$\frac{d\vec{h}_y}{dz} = -jk\vec{G}_e\vec{e}_x, \tag{8b}$$

with

$$\vec{B} = \vec{I} - \vec{Q}\vec{G}_o^{-1}\vec{Q}, \tag{9}$$

where $\vec{I}$ is an $s \times s$ identity matrix, and $\vec{Q}$ is an $s \times s$ diagonal matrices with on-diagonal elements $q_{rr} = \sigma_i$; $\vec{G}_o^{-1}$ is the inverse matrix of $\vec{G}_o$, and $\vec{G}_o$ and $\vec{G}_e$ are the $s \times s$ Fourier coefficient matrices of ordinary and extraordinary relative permittivities, respectively, which are given by

$$\vec{\Gamma} = \begin{bmatrix} \hat{\gamma}_0 & \hat{\gamma}_{-1} & \hat{\gamma}_{-2} & \cdots & \hat{\gamma}_{-s+1} \\ \hat{\gamma}_1 & \hat{\gamma}_0 & \hat{\gamma}_{-1} & \cdots & \hat{\gamma}_{-s+2} \\ \cdots & \cdots & \cdots & \cdots & \cdots \\ \hat{\gamma}_{s-1} & \hat{\gamma}_{s-2} & \hat{\gamma}_{s-3} & \cdots & \hat{\gamma}_0 \end{bmatrix}. \tag{10}$$

In (10), $\vec{\Gamma} = \vec{G}_o$ if $\hat{\gamma}_j = \hat{\epsilon}_j$, or $\vec{\Gamma} = \vec{G}_e$ if $\hat{\gamma}_j = \hat{\kappa}_j$. If we next define a $2s$-dimensional column vector $\vec{S}(z)$:

$$\vec{S}(z) = \begin{bmatrix} \vec{e}_x(z) \\ \vec{h}_y(z) \end{bmatrix}, \tag{11}$$

then (8) can be expressed in a matrix form as

$$\frac{d\vec{S}(z)}{dz} = -jk\vec{A}\vec{S}(z) \tag{12}$$

with

$$\vec{A} = \begin{bmatrix} \vec{0} & \vec{B} \\ \vec{G}_e & \vec{0} \end{bmatrix}, \tag{13}$$

where $\vec{A}$ is a $2s \times 2s$ coefficient matrix and $\vec{0}$ is an $s \times s$ zero matrix. State equations (12) have solutions in the form

$$\vec{S}(z + z') = e^{-j\vec{A}kz}\,\vec{S}(z'), \tag{14}$$

where $z'$ is an arbitrary initial value of $z$ inside a slab grating.

From here on, we use the index $n$ wherever necessary to indicate the $n$th layer. The continuity of tangential electromagnetic fields at $z = z_n$ yields

$$\vec{S}_{n+1}(z_n) = \vec{S}_n(z_n). \tag{15}$$

Also, from (14) we have

$$\vec{S}_n(z_n) = \vec{S}_n(z_{n-1} + z_0) = e^{-j\vec{A}kz_0}\,\vec{S}_n(z_{n-1}), \tag{16}$$

where $z_0$ is the thickness of each layer. Applying (15) and (16) continuously to the $N$ layers, where $N$ is the total number of decomposed layers in the grating region (region 2 in Fig. 1 *a*), we obtain

$$\vec{S}_N(d) = [e^{-j\vec{A}_N kz_0} e^{-j\vec{A}_{N-1}kz_0} \cdots e^{-j\vec{A}_1 kz_0}]\vec{S}_1(0) = \vec{P}\vec{S}_1(0), \tag{17}$$

where $\vec{P}$ is a propagation matrix that relates the amplitudes of space harmonics at $z = 0$ to that at $z = d$, and $d$ is the total thickness of the grating.

When illuminated by an obliquely incident, linearly polarized plane wave, the periodic structure produces reflected and transmitted waves, or equivalently backward and forward diffracted orders, in the upper and lower bounding regions (regions 1 and 3 in Fig. 1 *a*). Thus, the total magnetic fields in two bounding regions can be expressed as

$$H_{y1} = \sqrt{\frac{\epsilon_o}{\mu_o}}\left[e^{-jn_1 k(\sin\omega_1 x + \cos\omega_1 z)} + \sum_{i=-\infty}^{+\infty} R_i e^{-jk(\sigma_i x - \beta_{1i} z)}\right], \tag{18a}$$

$$H_{y3} = \sqrt{\frac{\epsilon_o}{\mu_o}} \sum_{i=-\infty}^{+\infty} T_i e^{-jk[\sigma_i x + \beta_{3i}(z-d)]}, \tag{18b}$$

where

$$\beta_{1i} = \begin{cases} (\epsilon_1 - \sigma_i^2)^{1/2}, & \text{for } \epsilon_1 > \sigma_i^2 \\ -j(\sigma_i^2 - \epsilon_1)^{1/2}, & \text{for } \epsilon_1 < \sigma_i^2 \end{cases}, \tag{19a}$$

$$\beta_{3i} = \begin{cases} (\epsilon_3 - \sigma_i^2)^{1/2}, & \text{for } \epsilon_3 > \sigma_i^2 \\ -j(\sigma_i^2 - \epsilon_3)^{1/2}, & \text{for } \epsilon_3 < \sigma_i^2 \end{cases}, \tag{19b}$$

$R_i$ and $T_i$ are the normalized amplitudes of the reflected and transmitted diffraction orders, and $\epsilon_1 = n_1^2$ and $\epsilon_3 = n_3^2$ are the relative permittivities of regions 1 and 3 ($n_3$ is the refractive index of region 3), respectively. The $E_x$ of region 1 and region 3 can be obtained from (18) and (1b) using the appropriate relative permittivities. Applying the boundary conditions on $E_x$ and $H_y$ at $z = 0$ yields

$$h_{r,1}(0) = \delta_{i0} + R_r, \tag{20a}$$

$$e_{r,1}(0) = \frac{1}{\epsilon_1 k}(k_{1z}\delta_{i0} - k_{1zi}R_r), \tag{20b}$$

and that at $z = d$ yields

$$h_{r,N}(d) = T_r, \tag{21a}$$

$$e_{r,N}(d) = \frac{k_{3zi}}{\epsilon_3 k} T_r. \tag{21b}$$

If $R_i$ and $T_i$ are eliminated from (20) and (21), the resultant equations reduce to two sets, which in a matrix form can be written as

$$\begin{bmatrix} \vec{E} & \vec{0} \\ \vec{0} & \vec{F} \end{bmatrix}\begin{bmatrix} \vec{S}_1(0) \\ \vec{S}_N(d) \end{bmatrix} = \begin{bmatrix} \vec{U} \\ \vec{Z} \end{bmatrix}, \tag{22}$$

with

$$\vec{E} = [\vec{I} \quad \vec{E}'], \qquad \vec{F} = [\vec{I} - \vec{F}'], \tag{23}$$

where $\vec{E}'$ and $\vec{F}'$ are the $s \times s$ diagonal matrices with on-diagonal elements $e_{rr} = \beta_{1i}/\epsilon_1$ and $f_{rr} = \beta_{3i}/\epsilon_3$, respectively; $\vec{Z}$ is an $s$-dimensional zero column vector, and $\vec{U}$ is an $s$-dimensional column vector with each component equal to $u_r = (2\cos\omega_1/n_1)\delta_{i0}$, where $\delta_{i0} = 1$ for $i = 0$ and $\delta_{i0} = 0$ for $i \neq 0$. Note that all of the components of $\vec{U}$ are equal to zero except the one corresponding to $i = 0$. Substitution of $\vec{S}_N(d)$ in (17) into (22) yields

$$\begin{bmatrix} \vec{E} \\ \vec{F}\vec{P} \end{bmatrix}\vec{S}_1(0) = \begin{bmatrix} \vec{U} \\ \vec{Z} \end{bmatrix}. \tag{24}$$

Equations 24 and 17 serve to determine $\vec{S}_1(0)$ and $\vec{S}_N(d)$, from which and from (20a) and (21a) $R_i$ and $T_i$ can be obtained.

The diffraction efficiencies in regions 1 and 3, $\eta_{1i}$ and $\eta_{3i}$, are defined as the diffracted power of a given order divided by the input power, and are obtained as

$$\eta_{1i} = \mathrm{Re}[\sqrt{\epsilon_1 - \sigma_i^2}]\frac{|R_i|^2}{n_1 \cos \omega_1}, \tag{25a}$$

$$\eta_{3i} = \mathrm{Re}[\sqrt{\epsilon_3 - \sigma_i^2}]\left(\frac{\epsilon_1}{\epsilon_3}\right)\frac{|T_i|^2}{n_1 \cos \omega_1}. \tag{25b}$$

Different implementations of the rigorous coupled-wave theory of grating diffraction are possible. For example, the theory can be implemented to analyze the diffraction characteristics of lossy surface-relief and metallic gratings or lossless dielectric gratings with small $\Lambda/\lambda$ ratios, in which case evanescent diffraction orders are of great importance. The evanescent orders have $\epsilon_1 < \sigma_i^2$ or $\epsilon_3 < \sigma_i^2$ in (19a) or (19b), and treating them in an algorithm requires special care. However, in the analysis of muscle fiber diffraction, it is unnecessary to include evanescent diffraction orders to obtain convergence in diffraction efficiency (this point will be confirmed with a numerical example in the following section). Therefore, the very simple algorithm described above can be used to analyze the muscle fiber diffraction accurately.

## Some remarks on numerical analysis

In our numerical analysis, we used the following parameters: $a = 1.6$ μm, $b = 1.9$ μm, $\zeta = 0.1$ μm, $d = 80$ μm, $z_0 = 1$ μm (the total layer number $N$ is 80), $n_1 = n_3 = 1.33$, and $\lambda = 0.633$ μm. The sarcomere length (grating period) $\Lambda$ is varied between 2.2 and 3.6 μm, which gives $\Delta x$ in the range 0–1.4 μm.

To show that evanescent orders are of very little importance in the analysis of muscle fiber diffraction, we employed a different implementation of the rigorous coupled-wave theory used to analyze lossy surface-relief gratings to the muscle fiber grating, and evaluated the diffraction efficiencies as functions of the number of diffraction orders retained in computation. The results obtained for the rectangular ($\delta x = 0$) grating of muscle fiber in relaxed state with $\Lambda = 2.2$ μm and $\omega_1 = 0°$ are shown in Fig. 3. Only the efficiencies of the undiffracted ($i = 0$) and the first-order ($i = +1$) diffracted waves in region 3 are presented. In this calculation, the normalized amplitudes of the input electric fields are set to 1 in both TE and TM cases. Similar results were obtained for other values of $\Lambda$ and for non-zero angles of incidence. As is seen from this figure, the efficiencies of the +1-order forward diffracted waves in both TE and TM polarizations converge if only 9 or more diffraction orders are retained in a computation. This is because in the muscle fiber, the differences of refractive indices of different subregions are small, and with $\lambda = 0.633$ μm, the $\Lambda/\lambda$ ratio is not too small. In a grating diffraction problem with normal incidence, the number of propagating diffraction orders (as opposed to evanescent diffraction orders), $N_p$, is determined by $N_p = 2n_p + 1$, where $n_p$ is an integer smaller than and

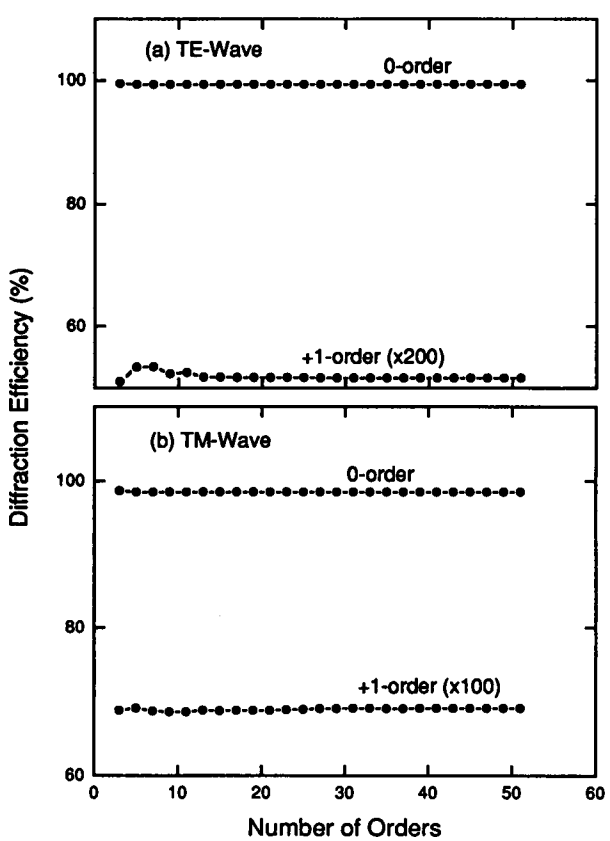


FIGURE 3 Diffraction efficiencies versus the number of orders retained in computations. Data presented are for the undiffracted ($i = 0$) and the first-order diffracted ($i = +1$) signals of (*top*) the transverse electric (TE) and (*bottom*) the transverse magnetic (TM) waves in region 3. Considered case is: relaxed state, normal incidence ($\omega_1 = 0°$), $\delta x = 0$ μm, $\delta(z) = 0$ μm and $\Lambda = 2.2$ μm.

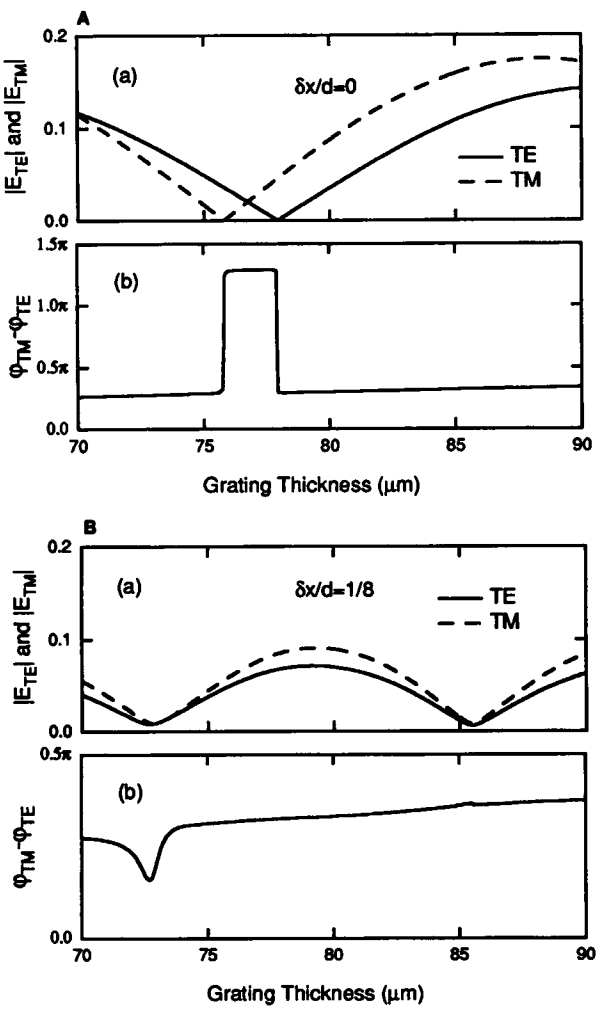


FIGURE 4 TE and TM field amplitudes of the first-order diffraction signals, and the differential phase shift between these two components, as functions of grating thickness for relaxed state, $\Lambda = 2.6$ μm, and $\delta(z) = 0$ μm. (*A*) $\delta x/d = 0$ (rectangular grating); (*B*) $\delta x/d = 1/8$ ($\delta x = 10$ μm for $d = 80$ μm).

closest to $n_1\Lambda/\lambda$ for region 1 and to $n_3\Lambda/\lambda$ for region 3. In our case $N_p$ = 9 for $\Lambda$ = 2.2 $\mu$m and $N_p$ = 11 for $\Lambda$ = 3.6 $\mu$m in both regions. In the subsequent numerical analyses in this paper, we used the simple algorithm described in the previous section with 9 diffraction orders.

We simulated the experiments (Chen, 1989) by introducing similar conditions into our numerical computations as were in the experiments. That is, (1) the angle of incidence was set to zero; (2) the normalized amplitudes of the input electric fields were set to 1 in both TE and TM cases; (3) the electric fields of the $i$ = +1 order forward diffracted waves at $z = d$, defined as

$$E_{TE} = [E_y(d)]_{i=+1} = |E_{TE}|\, e^{-j\varphi_{TE}}, \tag{26a}$$

$$E_{TM} = [E_x(d)]_{i=+1}/\cos\theta_D = |E_{TM}|\, e^{-j\varphi_{TM}}, \tag{26b}$$

were evaluated, where $\theta_D$ is the diffraction angle of the $i$ = +1 order at region 3; (4) the differential field ratio $r$ and total birefringence $\Delta n$, defined as

$$r = \frac{|E_{TM}| - |E_{TE}|}{|E_{TM}| + |E_{TE}|}, \tag{27a}$$

$$\Delta n = \frac{\varphi_{TM} - \varphi_{TE}}{kd}, \tag{27b}$$

were calculated. Note that the electric fields defined in (26) are unitless because they are calculated using corresponding input fields with normalized amplitudes. Among the numerical results to be presented, Figs. 4–7 were obtained for only the relaxed state of the muscle fiber, and the remaining Figs. 8 and 9 were for all three states, i.e., rigor, relaxed, and activated states.

## RESULTS

### Variation of the field parameters with myofibril skew

We first examined the properties of both the TE and the TM components of the first-order (+1) diffraction field components as they pass through a fiber (or grating) of a certain thickness. The conditions are $\Lambda$ = 2.6 $\mu$m and skew (or slippage) values of $\delta x/d$ = 0 (rectangular grating) and $\delta x/d$ = ⅛ ($\delta x$ = 10 $\mu$m over a fiber thickness of 80 $\mu$m). Fig. 4 *A* shows the field amplitudes (*a*) and phases (*b*) associated with TE and TM field components for the rectangular grating, $\delta x$ = 0 $\mu$m. Both the TE and the TM fields exhibit periodic variations in their amplitudes. There are dips to zero values at a certain well defined fiber thickness. These results were also noticed by other theoretical predictions using rigorous analysis techniques (Huxley, 1990; Thornhill et al., 1991; Sidick et al., 1992) so long as the fiber structure is rectangular. Note also that the difference in phase (Fig. 4 *A*(*b*)) between the two field components experiences a $\pi$-radian phase shift in the region formed by the two amplitude nulls. In Fig. 4 *B*, a slip plane value of $\delta x/d$ = 1/8 is imposed. We notice that the diffracted field amplitudes (Fig. 4 *B*(*a*)) no

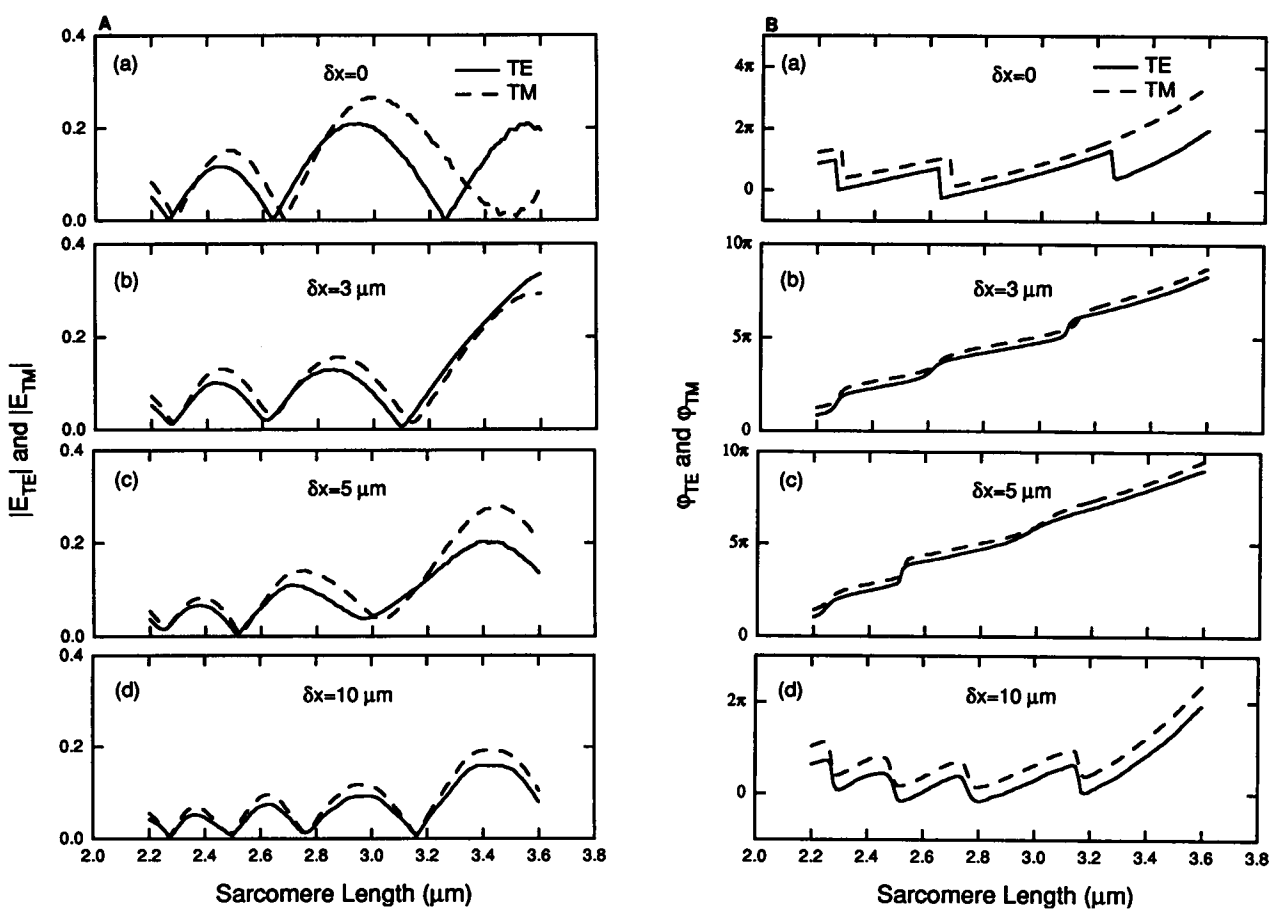


FIGURE 5 The TE and TM field amplitudes (*A*) and phases (*B*) of the first-order diffraction signals as a function of sarcomere length for four different cases of slip plane: $\delta x$ = 0, 3, 5, and 10 $\mu$m. In all cases, $d$ = 80 $\mu$m and $\delta(z)$ = 0 $\mu$m.

longer dip to zero values, and the fiber thicknesses at which the minima of the field amplitudes occur come closer to each other. Correspondingly, the differential phase shift (Fig. 4 *B*(*b*)) is much smaller. A minimum in the value of a field component at a specific value of fiber thickness implies destructive interference of that particular field component. The difference between the data of Fig. 4, *A* (rectangular grating) and *B* (with slip plane) shows that in the latter case, interference minima are no longer as sharp once skew of myofibrils exists. For the remaining model calculations, we have chosen a fiber thickness of 80 $\mu$m to be consistent with experimentally observed values.

We next varied sarcomere length $\Lambda$ for such a model fiber given varying degrees of myofibril skew or slippage. Results are shown in Fig. 5 *A* for the field amplitudes and in Fig. 5 *B* for the phases. Again, when the structure is regular with no skew or slippage, the two field components exhibit sharp amplitude difference reversals as $\Lambda$ is varied. This indicates that passage of light through such a material leads to abrupt changes in optical pathlength difference for the two field components. As the slip plane increases, the optical pathlength variation in space diminishes. As a result, difference in the field amplitudes decreases as does the phase shift differential. Fig. 5, *A*(*d*) and *B*(*d*) show that the curves with $\delta x = 10$ $\mu$m show little amplitude reversal and very little differential phase shift.

## Evaluation of differential field ratio *r* and birefringence ($\Delta n$)

For the following series of calculations, we use Eqs. 27a and b to convert the amplitudes and phases of the first-order TE and TM waves into the ellipsometry parameters *r* and $\Delta n$.

### *r and $\Delta n$ are plotted against $\Lambda$ with $\delta x$ as a parameter*

Consistent with the results displayed in Fig. 5, we note in Fig. 6 *A* that *r* exhibits strong oscillations in values as $\Lambda$ is varied if $\delta x = 0$ $\mu$m. In fact, it is almost as much negative as it is positive. The corresponding birefringence parameter $\Delta n$ shown in Fig. 6 *B* also shows abrupt changes in values indicating anomalous effects when the field components are strongly phase shifted. We noted that, for the analytical results to be more comparable to experimental data, $\delta x$ has to be increased. Indeed when $\delta x = 10$ $\mu$m, the anomalous regions are few and the calculated *r* and $\Delta n$ values become similar to those measured (Chen et al., 1989; Burton et al., 1990).

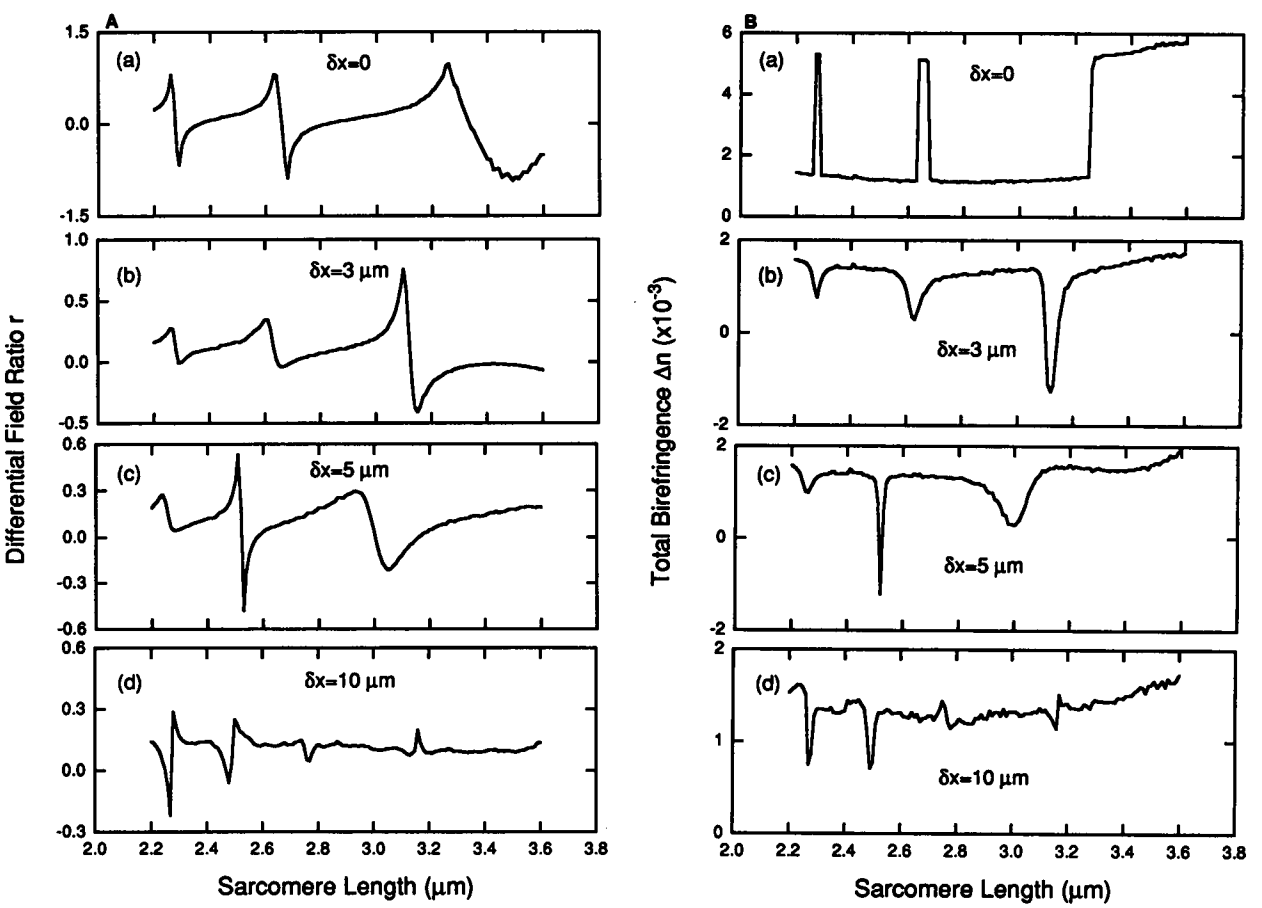


FIGURE 6 Dependence of (*A*) differential field ratio, *r*, and (*B*) total birefringence $\Delta n$, of the first-order diffraction signals on sarcomere length $\Lambda$ for four different cases of slip plane: $\delta x = 0$, 3, 5, and 10 $\mu$m. In all cases, $d = 80$ $\mu$m and $\delta(z) = 0$ $\mu$m.

*Having fixed slant $\delta x$ we next examine r and $\Delta n$ with the introduction of slip-plane randomness factor $\delta(z)$ as a parameter*

For this set of calculation, a random number generator is used to create the randomness factor $\delta(z) = \delta_0$ rand($z$) as we propagate through the layers of myofibrils. For each value of $\delta_0$ used, a set of $r$ and $\Delta n$ values is generated. Data presented with solid lines represent the average values of 100 sets of data, each of which is obtained using a different set of rand($z$) values. In Fig. 7, *A* and *B*, the maximum randomness parameter $\delta_0$ is increased from 0.01Λ to 0.10Λ. It can be seen that as randomness is increased, there is an apparent decrease in the sharp anomalous behaviors of both $r$ and $\Delta n$. The dotted curves indicate the SDs in $r$ and $\Delta n$ when the randomness is chosen as described. These SDs are seen to be rather large, again consistent with the experimental data of Chen et al. (1989) and Burton et al. (1990). This implies that if sampling were performed at different regions of a single fiber sample, or if experiments were conducted for different single fiber specimens, one would not be surprised to see results of $r$ and $\Delta n$ that vary quite substantially.

*Variation of the state of the fiber*

Because experimental data very seldom show anomalous swings in the values of either $r$ or $\Delta n$, we chose a particular set of slippage (or skew) and randomness parameters so that the correspondence to experiment is close. These values are $\delta x = 10$ μm and $\delta_0 = 0.03$ μm. In terms of Λ, the latter corresponds to $\delta_0 \approx 0.01\Lambda$. We next examined the differences in $r$ and $\Delta n$ of the different states of the fiber. Here we used the refractive indices of Table 1 to define the states of rigor, relaxed and activated fibers. In Fig. 8, *A* and *B*, the values of $r$ and $\Delta n$, each derived from 100 sets of data according to the protocol mentioned above, are plotted having used the conditions above. The use of $\delta_0 = 0.03$ μm certainly does not give rise to the smooth trends as shown in Fig. 7, $A(d)$ and $B(d)$. However, we believe that using a $\delta_0$ value larger than 0.03 μm is unrealistic. Our simulation condition corresponds to experimentally having selected a region of the fiber for study that is not very random (~1% of Λ) and making sure that it is always this region that is under scrutiny. In Fig. 9, the differences in both $r$ and $\Delta n$ among the three states are plotted using the average values of $r$ and $\Delta n$ shown

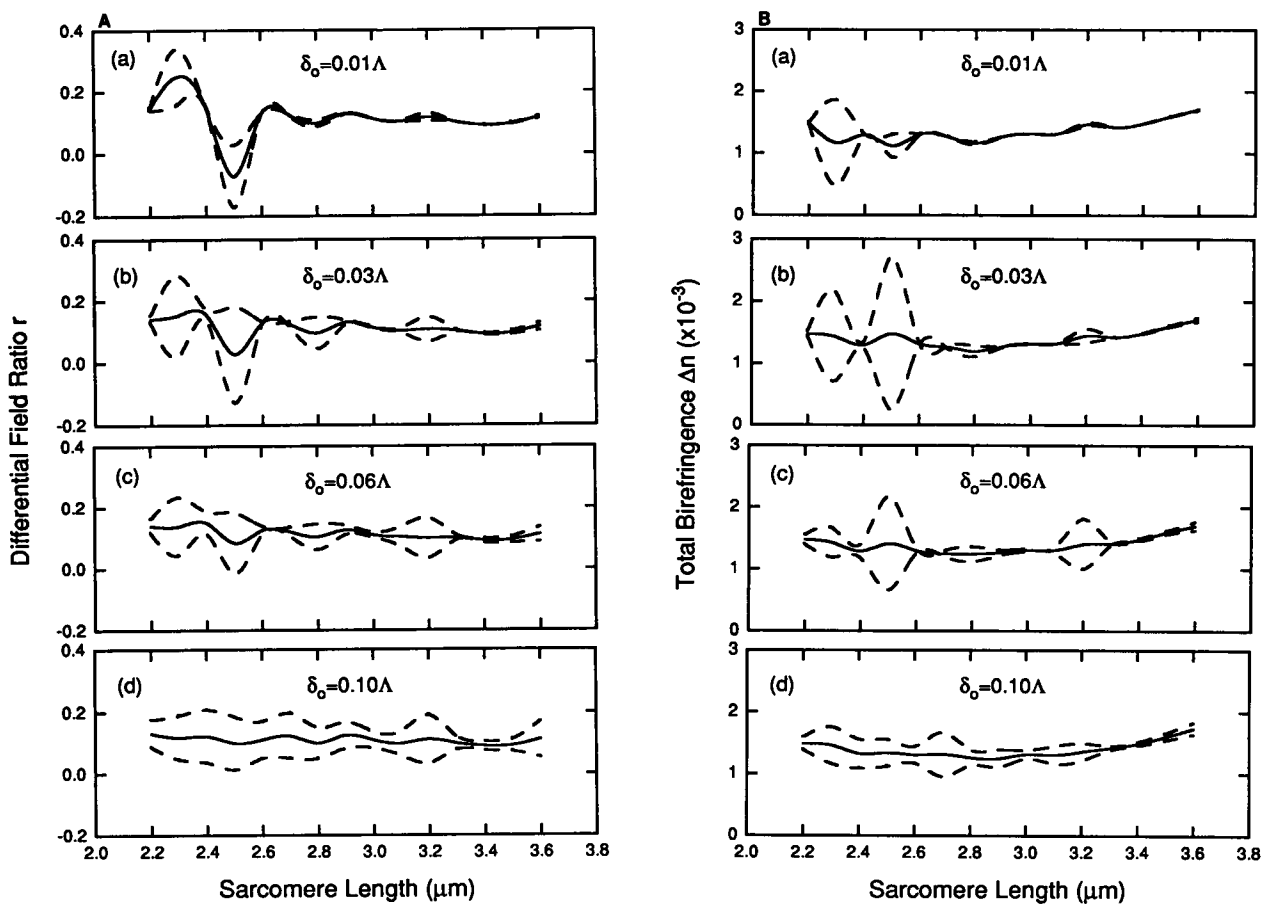


FIGURE 7 Dependence of (*A*) differential field ratio, $r$, and (*B*) total birefringence $\Delta n$, of the first-order diffraction signals on sarcomere length Λ for four different $\delta_0$ values: $\delta_0 = 0.01\Lambda$, $0.03\Lambda$, $0.06\Lambda$, and $0.1\Lambda$. The weighting parameter $\delta_0$ is related to other slip plane parameters by $u(z) = (\delta x/d)z + \delta(z)$ and $\delta(z) = \delta_0$ rand($z$), where $\delta x = 10$ μm, $d = 80$ μm, and rand($z$) is a random variable uniformly distributed in the interval [−½, ½]. For each value of $\delta_0$, 100 sets of $r$ and $\Delta n$ data were generated using different values of rand($z$). The solid lines represent the average values of those 100 sets of data, and the pairs of dashed lines show their standard deviations.

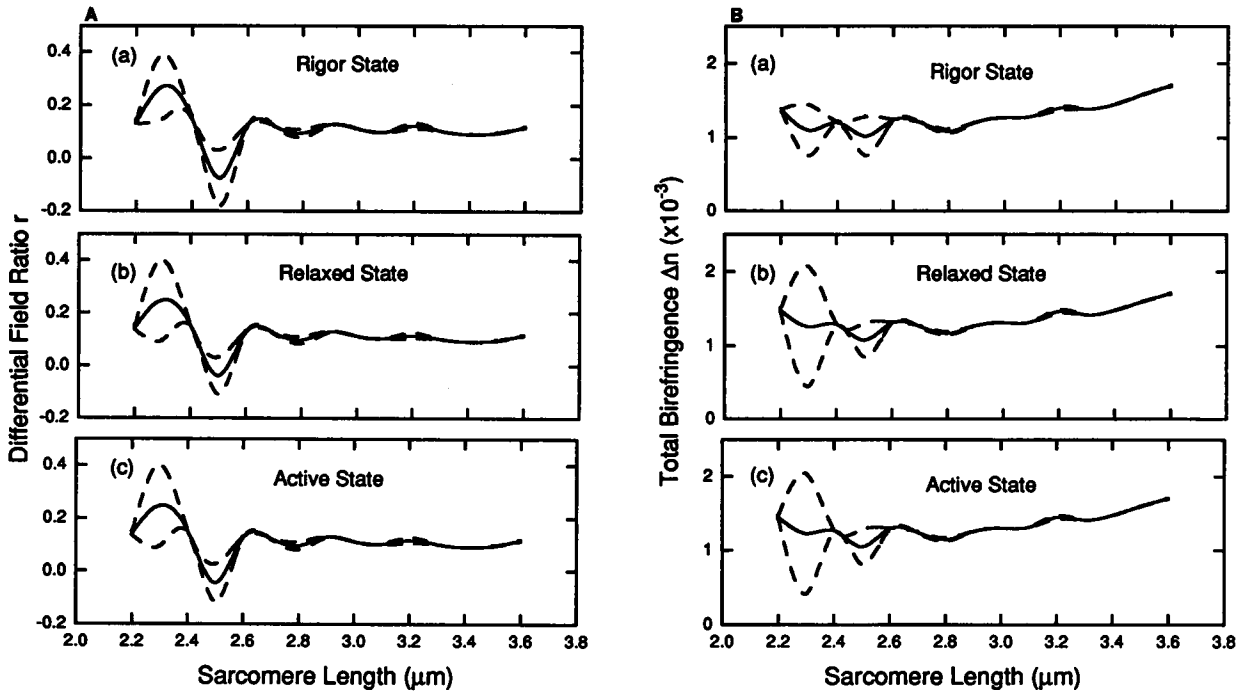


FIGURE 8 Same as Fig. 7, except that this figure is for three different fiber states: rigor, relaxed, and active, and that $\delta_0 = 0.03$ μm.

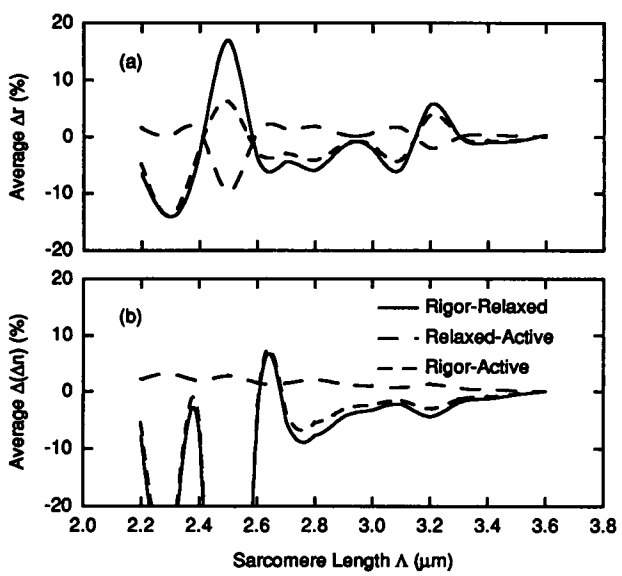


FIGURE 9 Changes in the differential field ratio, $r$, and the total birefringence, $\Delta n$, of the first-order diffraction signals as a function of sarcomere length $\Lambda$ for three different transitions: rigor-relaxed (*solid lines*), relaxed-active (*long dashed lines*), and rigor-active (*short dashed lines*). All the curves in this figure are obtained from the data represented by the solid lines in Fig. 8.

in Fig. 8, *A* and *B*. Each is a plot of $\Delta P = 100 \times (P_i - P_j)/P_i$, where $P = \{r, \Delta n\}$ and $i$ and $j$ are the states under consideration. From the $\Delta r$ values shown in Fig. 9 *a*, we see that there is a large, negative $\Delta r$ going from the rigor to the relaxed states. The $\Delta r$ values from the rigor to the active states are generally smaller but still negative. However, going from the relaxed to the active states yields a small but positive $\Delta r$. Fig. 9 *b* shows the corresponding trends in the changes of $\Delta n$. The results of these calculations are remarkably similar to experimental data reported earlier. With no adjustable parameters except those indicated, we see that the values of $r$ and $\Delta n$ are consistently largest for the relaxed state of the fiber. The rigor state has the smallest values, and the activated state has intermediate values. The absolute changes, up to ~13% at short $\Lambda$ and diminishing when $\Lambda = 3.6$ μm, in both $r$ and $\Delta n$, are very comparable to those observed experimentally.

## DISCUSSION

The rigorous coupled-wave theory has been extended to analyze both the TE and the TM polarization components of light diffracted from a model muscle fiber. As a result, this theory is able to handle material anisotropy in a most general way. There have been significant improvements of this theory over that which we previously developed (Yeh and Baskin, 1988). (1) This theory treats the problem of multiple scattering that occurs in any densely packed molecular or dielectric configuration. (2) The stratified myofibril model very closely resembles the geometrical structure of myofibrils in vitro and in vivo, complete with skew or slippage of adjacent myofibrils and the randomness associated with the average slip planes. (3) We have shown previously in (I) that the slip planes lead to a realistic account of the intensity differential between corresponding orders on the (+) and (−) sides of the forward transmitted beam of light. Here we showed that slip planes constitute a major factor in predicting the values of ellipsometric parameters $r$ and $\Delta n$. In particular, positive

or negative $r$ values can occur depending on the magnitude of the slip plane inclination. (4) Variation of myofibril alignment along the slip planes can lead to a highly varying set of values for both $r$ and $\Delta n$. It is only by locking onto a particular set of slab variations (myofibril variations) that one can obtain consistent trends in the values of $r$ and $\Delta n$ for state changes.

When a particular set of indices of refraction (Table 1) is introduced to represent the myofibril, we find that $r_{relaxed} > r_{active} > r_{rigor}$, and a corresponding trend in birefringence exists. Even more interesting is that the absolute values of both $r$ and $\Delta n$, as well as the trends in $\Lambda$ dependence of these two quantities are consistent with previously obtained experimental data, and there are no other adjustable parameters in this analysis. The careful numerical modeling experiments that we carried out here also show that data previously considered as showing large errors can now be fully explained. For example, in the work of Burton et al. (1990) the variations in $r$ as a function of sampling position along the fiber can be seen as the result of a variance in skew plane, something we had suspected without rigorous proof. In the work of Chen et al. (1989), the large error bars that were acquired by averaging data from different fibers are also consistent with the variance in myofibril slippage.

This model now has interpretative power in that experimental data can be fitted to the model parameters. In particular, the existence of slip planes and variations of the relative positions of myofibrils about the slip planes can be seen from the $\Lambda$ dependency of $r$ and $\Delta n$. The changes in $r$ and $\Delta n$ as a function of the changes in fiber states can be seen as specific changes in the regional indices of refraction. Thus, the results of diffraction ellipsometry performed at visible wavelengths can be interpreted on the basis of the controlled changes of molecular parameters representing the changes of states.

### *Limitations of sensitivity*

Fundamental to this analysis is the assumption that average values of indices of refraction exist within the different regions of a sarcomere. This macroscopic concept sets a limitation as to the spatial sensitivity of the technique. The specific values of these regional indices of refraction form the connection between microscopic molecular structures and macroscopic optical sampling. To be sure, spatial sampling is, at a minimum, over a region comparable to the wavelength of light. Changes in the structural features also must be averaged over the same spatial region. The fact that experimental data exist indicating 5–10% changes in the $r$ and the $\Delta n$ values under very well controlled conditions suggest that even within these scales of averaging, significant molecular changes can be detected. Accordingly, a rigorous coupled-wave analysis carried out to analyze data that are obtained under extreme care and control of parameters can be meaningful in characterizing the structures or changes of structures in the optical ellipsometry studies of muscle fibers.

One other limitation of this analysis is the assumption of principal axes representation for the myofibrils. Under the condition that the dielectric permitivity tensor is diagonal, there will not be any coupling between the TE and the TM modes. In a recent analysis by Yueh and Kong (1991), an intrinsically chiral grating was considered as the diffracting element. For the muscle fiber, if we use visible light with wavelengths far from the chiral absorption regions of the $\alpha$-helices (190–230 nm), the chiral contribution will be small. Other sources that can introduce errors to our assumption of a diagonal dielectric tensor include scattering contributions at the curved, cylindrical boundary structure between myofibrils. We have chosen to ignore these.

### *Relationship to other studies*

The principal unresolved problem in muscle biophysics is ascertaining the relationship between the structure of the molecular motor and force generation within the activation-contraction cycle. It has been established with a good degree of confidence that a single S-1 head can generate motor force (Harada et al., 1987; Toyoshima et al., 1987). Current emphasis is on the structure-function relationship of this molecular entity. Towards this end, direct electron microscopy of frozen hydrates of fibers immediately after flash release of caged ATP can now reveal the attitudes of cross-bridges at ~10 nm resolution (Hirose et al., 1993). Wakabayashi's group (Wakabayashi et al., 1992) have examined solution conformations of S-1 and showed that there could be structural changes in different states of the ATPase cycle. On the other hand, neutron scattering studies of S-1 in a solution of deuterated (therefore, invisible) actin filaments show that S-1 heads in the relaxed state and in the rigor state exhibit no major structural distinctions (Curmi et al., 1988). At present, even with the 2.8-Å resolution of the structure of myosin S-1, obtained by x-ray diffraction studies of the S-1 crystals (Rayment et al., 1993a), it is not possible as yet to rule out either interpretation based on the scattering data because in the model of Rayment et al. (1993b) the postulated change in structure during force generation is small. It is evident that time-dependent studies of the cross-bridge or S-1 over the course of a single ATPase cycle is needed. Irving et al. (1992) have recently shown, by correlating Huxley-Simmons tension transients with x-ray diffraction data, that myosin head movements are synchronous with the elementary force-generating process. Extrinsic probes such as fluorophores and spin labels that are sensitive to dynamics have provided strong evidence for microsecond time scale rotational disorder of the S-1 moiety during activation (Thomas, 1987). The information provided by these probes is very local, in the neighborhood of the probe molecule itself. What we have from optical ellipsometry data is that the changes in the diffracted signals are strongly indicative of definite and distinctive changes of the cross-bridge region in terms of indices of refraction. The same can be said of optical birefringence results of Peckham and Irving (1989). Although our resolution limit precludes our ascribing models of the S-1, on the

scale where we do have confidence, we can say that careful analysis applying this rigorous coupled-wave theory to experimental data and correlating data with those derived from probe experiments sensitive to very local structural changes will be useful in establishing the structure-function relationship that exists during the process of muscle contraction.

## REFERENCES


Baskin, R. J., Y. Yeh, K. Burton, J. S. Chen, and M. Jones. 1986. Optical depolarization changes in single, skinned muscle fibers: evidence for cross-bridge involvement. *Biophys. J.* 50:63–74.

Bragg, W. L., and A. B. Pippard. 1953. The form birefringence of macromolecules. *Acta Cryst.* 6:865–867.

Burton, K., R. J. Baskin, and Y. Yeh. 1990. Depolarization spectra of diffracted light: changes upon the stimulation of intact fiber. *J. Muscle Res Cell Motility* 11:258–270.

Chen, J. S., R. James Baskin, R. J. Baskin, S. Shen, Y. Yeh, and K. Burton. 1989. Polarization states of diffracted light: changes accompanying fiber activity. *Biophys. J.* 56:595–605.

Colby, R. H. 1971. Intrinsic birefringence of glycerinated myofibrils. *J. Cell Biol.* 51:763–771.

Curmi, P. M. G., D. B. Stone, D. K. Schneider, J. A. Spudich, and R. A. Mendelson. 1988. Comparison of the structure of myosin subfragment-1 bound to actin and free in solution: a neutron scattering study using actin made "invisible" by deuteration. *J. Mol. Biol.* 203:781–798.

Eberstein, A., and A. Rosenfalck. 1963. Birefringence of isolated muscle fibres in twitch and tetanus. *Acta Physiol. Scand.* 57:144–166.

Fajer, P. G., E. A. Fajer, and D. D. Thomas. 1990. Myosin heads have a broad orientational distribution during isometric muscle contraction. Time-resolved EPR studies using caged ATP. *Proc. Natl. Acad. Sci. USA.* 87:5538–5542.

Gaylord, T. K., and M. G. Moharam. 1985. Analysis and applications of optical diffraction by gratings. *Proc. IEEE.* 73:894–937.

Harada, Y., A. Noguchi, A. Kishino, and T. Yanagida. 1987. Sliding movement of single actin filaments on one-headed myosin filaments. *Nature.* 326:805–808.

Haskell, R. C., F. D. Carlson, and P. S. Blank. 1989. Form birefringence of muscle. *Biophys. J.* 56:401–413.

Hirose, K., T. D. Lenart, J. M. Muray, C. Franzini-Armstrong, and Y. E. Goldman. 1993. Flash and smash: rapid freezing of muscle fibers activated by photolysis of caged ATP. *Biophys. J.* 65:397–408.

Huxley, A. F., and R. Niedergerke. 1958. Measurement of the striations of isolated muscle fibres and the interference microscope. *J. Physiol.* 144: 403–425.

Huxley, A. F. 1990. A theoretical treatment of diffraction of light by a striated muscle fibre. *Proc. R. Soc. Lond. B.* 241:65–71.

Irving, M., V. Lombardi, G. Piazzesi, and M. A. Ferenczi. 1992. Myosin head movements are synchronized with elementary force-generating process in muscle. *Nature.* 357:156–158.

Irving, M., M. Peckham, and M. A. Ferenczi. 1987. Birefringence as a probe of crossbridge orientation in demembranated muscle fibres. *In* Molecular Mechanisms of Muscle Contraction. H. Sugi and G. H. Hollack, editors. Plenum Press, New York. 299–306.

Jones, M., R. J. Baskin, and Y. Yeh. 1991. The molecular origin of birefringence in skeletal muscle: contribution of myosin subfragment S-1. *Biophys. J.* 60:1217–1228.

Leung, A. F. 1987. Degree of polarization of light diffracted from resting striated muscle. *Cell Biophys.* 10:145–168.

Leung, A. F., and M. K. Cheung. 1987. Polarization changes in light diffracted from contracting muscle fibers. *Cell Biophys.* 10:127–144.

Moharam, M. G., and T. K. Gaylord. 1982. Diffraction analysis of dielectric surface-relief gratings. *J. Opt. Soc. Amer.* 72:1385–1392.

Moharam, M. G., and T. K. Gaylord. 1983. Three-dimensional vector coupled-wave analysis of planar-grating diffraction. *J. Opt. Soc. Amer.* 73:1105–1112.

Peckham, M., and M. Irving. 1989. Myosin crossbridge orientation in demembranated muscle fibres studied by birefringence and x-ray diffraction measurements. *J. Mol. Biol.* 210:113–126.

Pollard, T. D., D. Bhandari, P. Maupin, D. Wachsstock, A. G. Weeds, and H. G. Zot. 1993. Direct visualization by electron microscopy of the weakly bound intermediates in the actomyosin adenosine triphosphatase cycle. *Biophys. J.* 64:454–471.

Rayment, I., H. M. Holden, M. Whittaker, C. B. Yohn, M. Lorenz, K. C. Holmes, and R. A. Milligan. 1993a. Structure of the actin-myosin complex and its implications for muscle contraction. *Science.* 261:58–65.

Rayment, I., W. R. Rypniewski, K. Schmidt-Base, R. Smith, D. R. Tomchick, M. M. Benning, D. A. Winkelmann, G. Wesenberg, and H. M. Holden. 1993b. Three-dimensional structure of myosin subfragment-1: a molecular motor. *Science.* 261:50–58.

Sidick, E., A. Knoesen, J. K. Xian, Y. Yeh, and R. J. Baskin. 1992. Rigorous analysis of light diffraction by a striated muscle fibre. *Proc. R. Soc. Lond. B.* 249:247–257.

Taylor, D. L. 1975. Birefringence changes in vertebrate striated muscle. *J. Supramol. Struct.* 3:181–191.

Thomas, D. D. 1987. Spectroscopic probes of muscle crossbridge rotation. *Annu. Rev. Physiol.* 49:891–909.

Thornhill, R. A., N. Thomas, and N. Berovic. 1991. Optical diffraction by well-ordered muscle fibres. *Eur. Biophys. J.* 20:87–99.

Toyoshima, Y. Y., S. J. Kron, and J. A. Spudich. 1990. The myosin step size: Measurement of the unit displacement per ATP hydrolyzed in an in vitro assay. *Proc. Natl. Acad. Sci. USA.* 87:7130–7134.

Wakabayashi, K., M. Tokunaga, I. Kohno, Y. Sugimoto, T. Hamanaka, Y. Takezawa, T. Wakabayashi, and Y. Amemiya. 1992. Small-angle synchrotron x-ray scattering reveals distinct chape changes of the myosin head during hydrolysis of ATP. *Science.* 258:443–447.

Yeh, Y., M. E. Corcoran, R. J. Baskin, and R. L. Lieber. 1983. Optical depolarization changes on the diffraction pattern in the transition of skinned muscle fibers from relaxed to rigor state. *Biophys. J.* 44:343–351.

Yeh, Y., R. J. Baskin, R. A. Brown, and K. Burton. 1985. Depolarization spectrum of diffracted light from muscle fiber: the intrinsic anisotropy component. *Biophys. J.* 47:739–742.

Yeh, Y., and R. J. Baskin. 1988. Theory of optical ellipsometry from muscle fibers. *Biophys. J.* 54:205–218.

Yueh, S. H., and J. A. Kong. 1991. Analysis of diffraction from chiral gratings. *J. Electromagnetic Waves and Applications* 5:701–714.